CHEMISTRY OF MATERIALS

pubs.acs.org/cm

Article

# Interfacial Degradation Mechanism of Nanostructured $LiCoO_2$ for $Li_6PS_5Cl$-Based All-Solid-State Batteries

Kanghyeon Kim,[§] Seunggoo Jun,[§] Taehun Kim, Jong Seok Kim, Seonghyun Lee, Gawon Song, Junsung Park, Yoon Seok Jung,* and Kyu Tae Lee*

Cite This: *Chem. Mater.* 2024, 36, 5215−5227

Read Online

ACCESS | Metrics & More | Article Recommendations | Supporting Information

**ABSTRACT:** Interfacial degradation of $Li_6PS_5Cl$ (LPSCl) with oxide cathode materials during cycling, particularly the formation of interfacial voids, leads to poor electrochemical performance. The formation of these voids is driven by two distinct mechanisms: the volumetric changes of oxide cathode materials during cycling and the volumetric shrinkage of LPSCl due to oxidative decomposition. However, the relative contribution of each route to void formation remains ambiguous, especially for nanostructured cathode materials. This study highlights the predominant influence of oxidative decomposition of LPSCl on the nanostructured $LiCoO_2$ surface in the formation of interfacial voids when compared to the volumetric changes of $LiCoO_2$ between charging and discharging. The interfacial degradation behavior is compared between bare $LiCoO_2$ and $LiCoO_2$−$Li_2SnO_3$ core−shell nanoparticles. Both types of nanoparticles exhibit comparable absolute volume changes of $LiCoO_2$ during cycling, due to their similar particle sizes and reversible capacities, effectively ruling out the impact of volumetric changes of $LiCoO_2$ on void formation. However, $LiCoO_2$−$Li_2SnO_3$ shows mitigated interfacial void formation compared to bare $LiCoO_2$, resulting in improved electrochemical performance. This is attributed to the fact that $LiCoO_2$−$Li_2SnO_3$ suppresses the oxidative decomposition of LPSCl due to the enhanced chemical stability of $Li_2SnO_3$ with LPSCl. This reveals that the oxidative decomposition of LPSCl on the nanostructured $LiCoO_2$ surface contributes more significantly to void formation than the volume change of $LiCoO_2$. These findings provide valuable insights into the degradation mechanisms of nanostructured cathode materials.

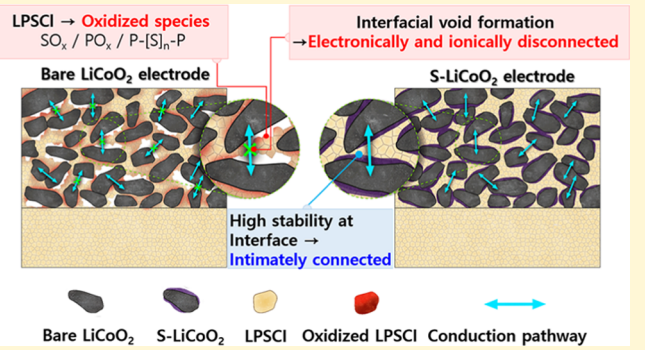


## 1. INTRODUCTION

Lithium-ion battery (LIB) technology, typically reliant on organic solvent-based electrolytes, currently confronts challenges in simultaneously achieving high energy density and safety for electric vehicles. To tackle these issues, there is a growing interest in transitioning from conventional LIBs to the next generation of all-solid-state batteries (ASSBs) using solid electrolytes.[1,2] Although various solid electrolytes, including oxide, sulfide, and polymer-based ionic conductors, have been explored for ASSBs, thiophosphate-based solid electrolytes, such as $Li_6PS_5Cl$ (LPSCl), have attracted intensive attention due to their mechanical flexibility, high ionic conductivity, and manufacturability.[3−5] However, the transition to ASSBs also encounters difficulties related to structural and mechanical degradation at the interface between thiophosphate solid electrolytes and layered oxide-based cathode materials. This gradual interfacial degradation during cycling gives rise to an increasing charge-transfer resistance and, eventually, poor capacity retention.[6−13]

The interfacial degradation of the cathode in LPSCl-based ASSBs is predominantly attributed to the narrow electrochemical stability window of LPSCl and the volume change of oxide cathode materials during charging and discharging, as illustrated in Scheme 1. First, the reductive and oxidative decomposition of LPSCl at the interface between LPSCl and the oxide cathode leads to the formation of a passivation layer on the oxide cathode surface.[8,14,15] This layer is composed of sulfate, phosphate, and polysulfide.[15,16] The accumulation of these passivation layers during cycling impedes the kinetics of charge transfer, resulting in an increase in interfacial resistance. Second, mechanical degradation of the electrode, such as void formation at the interface, occurs during cycling, which leads to the loss of ionic and electronic contact of active materials.[9,17−20] Layered oxide cathode materials, such as $LiCoO_2$ and $Li[Ni_{1-x-y}Co_xMn_y]O_2$, undergo a volume change of approximately 2−7% during charging and discharging.[21−23] This volume strain accelerates the fatigue of not only the

Received: March 4, 2024
Revised: May 1, 2024
Accepted: May 1, 2024
Published: May 8, 2024

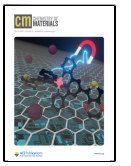

**Scheme 1. Schematic Illustration of the Interfacial Degradation Modes of LPSCl at the Cathode Surface in LPSCl-Based ASSBs**

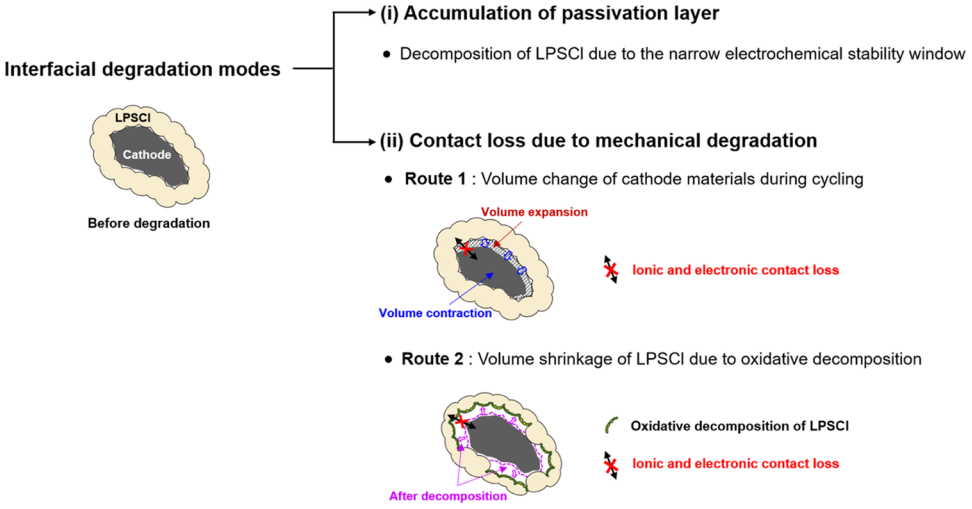


powder but also the electrode, eventually causing both the pulverization of polycrystalline oxide particles due to intergranular crack formation and the formation of interfacial voids between the oxide cathode particles and LPSCl particles.[17,24−26] In addition to the volume change of oxide cathode materials, LPSCl itself undergoes irreversible volume shrinkage during charging, which leads to the formation of interfacial voids. The oxidative decomposition of LPSCl during charging is known to occur as follows[8,27,28]

$$Li_6PS_5Cl \rightarrow LiCl + \frac{1}{2}P_2S_5 + \frac{5}{2}S + 5Li^+ + 5e^- \quad (1)$$

The molar volumes of LPSCl and its oxidative decomposition products, consisting of LiCl, $P_2S_5$, and S, are 163.64 and 114.55 mL $mol^{-1}$, respectively. This indicates that the partial volume of LPSCl in the cathode electrode significantly shrinks due to electrochemical oxidative decomposition during charging. As a result, voids form at the interface between LPSCl powders and oxide cathode powders. Moreover, chemical oxidation of LPSCl on the cathode surface also contributes to accelerating interfacial void formation. The resulting oxidative decomposition products of LPSCl, including sulfates and phosphates, exhibit increased brittleness and a higher Young's modulus due to changes in bond dissociation energy and ion packing density compared to pristine LPSCl.[29−31] This increased brittleness and stiffness pose challenges in maintaining contact between oxide cathode particles and LPSCl particles, particularly during volume changes in the repeated charge and discharge processes. Since void formation at the interface disrupts the intimate contact between LPSCl and oxide cathode particles, the electrochemical performance of LPSCl is significantly influenced by interfacial void formation.[20] However, although previous literature has proposed two routes for interfacial void formation—(i) volume change of oxide cathode materials during cycling and (ii) volume shrinkage of LPSCl due to oxidative decomposition—the critical contribution of each route to interfacial void formation remains ambiguous.[32−36] This lack of clarity is attributed to the difficulty in isolating the individual effects of these routes during cycling, as both occur simultaneously in conventional systems. Moreover, there has been limited exploration into the interfacial failure modes of nanostructured cathode materials, especially in relation to the electrochemical decomposition of LPSCl on the cathode surface as compared to the volume changes of active materials.[10,11] In this regard, a comparative analysis of this aspect is essential for enhancing the electrochemical performance of nanostructured electrode materials in ASSBs.

In this study, we elucidated the significant role of the oxidative decomposition of LPSCl on the nanostructured $LiCoO_2$ surface in contributing to interfacial void formation, relative to the volume changes of $LiCoO_2$ during charging and discharging. We compared the interfacial degradation behavior between bare $LiCoO_2$ and $LiCoO_2$−$Li_2SnO_3$ core−shell nanoparticles. Given that both types of nanoparticles exhibited similar particle size distributions and reversible capacities, we inferred that they undergo comparable absolute volume changes of $LiCoO_2$ during charging and discharging. However, $Li_2SnO_3$ demonstrated enhanced chemical stability with LPSCl compared to $LiCoO_2$. For this reason, nanostructured $LiCoO_2$−$Li_2SnO_3$ significantly mitigated the oxidative decomposition of LPSCl on the cathode surface in contrast to bare $LiCoO_2$, thereby suppressing interfacial void formation. Consequently, $LiCoO_2$−$Li_2SnO_3$ exhibited reduced formation of electrochemically inactive dead volume within the composite cathode during cycling, leading to improved electrochemical performance. This finding emphasizes the critical role of oxidative decomposition of LPSCl in the cell failure of nanostructured $LiCoO_2$.

## 2. EXPERIMENTAL SECTION

**2.1. Synthesis of Materials.** Bare $LiCoO_2$ and surface-regulated $LiCoO_2$−$Li_2SnO_3$ core−shell nanoparticles were synthesized through a sol−gel method. The precursors, including $LiNO_3$ (Aldrich, 99%), $Co(NO_3)_2{\cdot}6H_2O$ (Aldrich, 98%), and $SnCl_2$ (Alfa, 98%), were dissolved in ethanol. The molar ratio of the precursors was Li/Co/Sn = $1.03(1 + x):x:1 - x$, where $x = 0$ for bare $LiCoO_2$ and 0.05 for $LiCoO_2$−$Li_2SnO_3$ core−shell. To chelate all of the cations, citric acid (Aldrich, 99%) was added to the mixture. The resulting solutions were stirred for 3 days at 60 °C to obtain highly viscous gels, which were then dried in a vacuum oven at 80 °C overnight. The obtained powders were heated in air at 300 °C for 5 h to induce combustion and then further heated in air at 900 °C for 10 h. During heating, Sn-doped $LiCoO_2$ initially formed below 900 °C. This was followed by the plane-selective phase segregation of Sn-doped $LiCoO_2$ into


https://doi.org/10.1021/acs.chemmater.4c00629
Chem. Mater. 2024, 36, 5215−5227

$LiCoO_2$−$Li_2SnO_3$ core−shell at 900 °C, due to the thermodynamic instability of Sn-doped $LiCoO_2$ at this temperature. $Li_2SnO_3$ powders were synthesized through a solid-state method. The mixture of tin oxalate (Aldrich, 98%) and $Li_2CO_3$ (Aldrich, 99%) was calcined at 800 °C for 3 h under an oxygen atmosphere with heating and cooling rates of 2 °C $min^{-1}$. For the synthesis of $Li_3YCl_6$ powders, mechanical ball milling was carried out using a mixture of LiCl (Alfa, 99.9%) and $YCl_3$ (Alfa, 99.999%). The mechanochemical milling was performed at 500 rpm for 20 h with 10 mm $ZrO_2$ balls (10 mm $ZrO_2$ ball/precursor powder = 30:1 as a mass ratio). Prior to use, all powders, except for the solid electrolytes, were dried in a vacuum oven at 200 °C. All chemicals were stored in an Ar-filled glovebox with an oxygen concentration of less than 0.5 ppm and a water concentration of less than 0.1 ppm.

**2.2. Cell Fabrication for All-Solid-State Batteries.** All-solid-state cells consisted of trilayers: a composite cathode pellet, a solid electrolyte pellet, and an anode. For the preparation of the composite cathode, $LiCoO_2$ and LPSCl powders were mixed with a weight ratio of $LiCoO_2$/LPSCl = 13:7. A Li metal foil (100 $\mu$m in thickness, Honjo, Japan), a lithium−indium (Li−In) alloy, and a $Li_4Ti_5O_{12}$ composite anode were utilized as anode electrodes, depending on the purposes of the electrochemical cells. (i) Li metal was used as the anode when evaluating the electrochemical performance of $LiCoO_2$ (Li|LPSCl|$LiCoO_2$), (ii) the Li−In alloy was used as the anode for in situ X-ray diffraction (XRD) and in situ electronic resistance measurement (Li−In|LPSCl|$LiCoO_2$), and (iii) $Li_4Ti_5O_{12}$ was used as the anode for operando electrochemical pressiometry measurements ($Li_4Ti_5O_{12}$|LPSCl|$LiCoO_2$) because $Li_4Ti_5O_{12}$ is a zero-strain material. The Li−In alloy electrodes were prepared by laminating Li metal (20 $\mu$m in thickness, Honjo, Japan) and indium metal (50 $\mu$m in thickness, MTI Korea Co.). The $Li_4Ti_5O_{12}$ composite anode was prepared by using $Li_4Ti_5O_{12}$, LPSCl, carbon additives (Super C65), and solvate ionic liquid (Li(G3)TFSI, where LiTFSI = lithium bis(trifluoromethanesulfonyl)imide) and G3 = triethylene glycol dimethyl ether in a weight ratio of 10:9:1:0.1.

We assembled the bulk-type cells to evaluate the electrochemical performance of ASSBs as follows. The bulk-type cells feature a cell configuration of Li|LPSCl|$LiCoO_2$. The solid electrolyte layer was initially prepared by pelletizing 150 mg of LPSCl at 145 MPa. Subsequently, composite cathode powders were evenly spread onto the solid electrolyte pellet and pressed at 360 MPa. The mass loading of $LiCoO_2$ was approximately 7.35 mg $cm^{-2}$. The composite cathode was approximately 45 $\mu$m in thickness and 1.3 cm in diameter. A metal foil was then attached to the other side of the solid electrolyte layer pellet. The bulk-type cell assembly involved applying a torque of 5 Nm. No additional pressure was applied during cycling. The homemade cells were assembled applying a torque of 10 Nm for in situ XRD and operando electrochemical pressiometry analyses. No additional pressure was applied during cycling. For operando electrochemical pressiometry, the $Li_4Ti_5O_{12}$ composite anode powders were pressed at 360 MPa, with a mass loading of approximately 8.06 mg $cm^{-2}$.

**2.3. Material Characterization.** Structural characterizations were conducted via powder X-ray diffraction (XRD) measurement using a Bruker D2 PHASER instrument with Cu K$\alpha$ radiation ($\lambda$ = 1.5418 Å). For ex situ XRD analysis, the electrodes retrieved from the bulk-type cell after cycling were mounted on the specimen holder and sealed with a beryllium window. For in situ XRD analysis, the data were continuously collected with a step size of 0.02° using a Rigaku MiniFlex 600 diffractometer equipped with Cu K$\alpha$ radiation. Scanning electron microscopy (SEM) images were acquired with a field emission scanning electron microscope (Carl Zeiss, AURIGA, Germany). To obtain cross-sectional SEM and energy-dispersive X-ray spectroscopy (EDS) mapping images of $LiCoO_2$−$Li_2SnO_3$ core−shell nanoparticles, the powder was mixed with poly(vinylidene fluoride) (PVDF) binder in an *N*-methyl-2-pyrrolidone (NMP) solution and cast on an Al foil, followed by drying. The resulting sample film was then polished with an Ar-ion beam using a cross section polisher (JEOL, SM-09010). For the cross-sectional SEM images of ASSBs before and after cycling, the bulk-type cells were first disassembled in an Ar-filled glovebox to retrieve the composite cathode. Subsequently, the composite cathode pellets were polished with an Ar-ion beam using a cooling cross section polisher (JEOL, IB-19520CCP) at optimized current and −100 °C. The sample specimens were then transferred to the SEM instrument using an airtight sealed transfer vessel. Transmission electron microscope (TEM) and EDS mapping images were collected using a Cs-corrected scanning transmission electron microscope (JEOL Ltd., JEM-ARM200F). Cross-sectional specimens were prepared using a focused ion beam (FIB) milling (JEOL Ltd., JEM-F200). Particle size distribution (PSD) was measured using a Microtrac S3500 particle size analyzer. Raman spectra were collected using a RAMAN spectrometer II (DXR2xi). An airtight sealed cell was employed for examining samples containing air-sensitive powders. X-ray photoelectron spectroscopy (XPS) analysis was performed using a Versaprobe III instrument (UL-PHI) with monochromatic Al K$\alpha$ radiation (1486.7 eV) and a 100 $\mu$m beam diameter at a power of 25 W and 15 keV. All samples were transferred to the XPS instrument using an airtight sealed transfer vessel. XPS spectra were calibrated using the signal of carbon at 284.8 eV. Time-of-flight secondary-ion mass spectrometry (TOF-SIMS) analysis was performed in a negative ion mode using a TOF.SIMS 5 instrument (ION-TOF, Germany) with a 30 keV $Bi^+$ primary ion source. Samples were transferred to the analysis chamber using an airtight sealed transfer vessel (ION-TOF, Germany). Analyses were run until a dose density limit of $1.0 \times 10^{13}$ ions $cm^{-2}$ was reached for the analysis area of 100 × 100 $\mu m^2$.

**2.4. Electrochemical Characterization.** Cycle performance of Li|LPSCl|$LiCoO_2$ cells was evaluated using TOSCAT-3100 battery cycler (TOYO, Japan). The bulk-type cells were charged and discharged at 0.1C and 30 °C. 1C corresponds to 1.2 mA $cm^{-2}$. Charging was carried out using a constant current/constant voltage (CC/CV) mode, during which the cell voltage was held at 4.3 V (vs $Li^+$/Li) until current density decayed to 0.05C. Rate performance was examined by discharging the cells at various current densities while charging them at a consistent current density of 0.1C, using the CC/CV mode in the voltage range of 2.5−4.3 V (vs $Li^+$/Li) at 30 °C. For the galvanostatic intermittent titration technique (GITT), a constant current density of 0.1C was applied for 10 min, followed by allowing the cell to rest for 50 min to reach a quasi-equilibrium state. Electrochemical impedance spectroscopy (EIS) was conducted using an SP-150 potentiostat (Biologic, France). EIS analysis was performed by applying a 10 mV amplitude in a frequency range of 1 MHz−10 mHz, with 20 data points per decade of frequency at room temperature. EIS analysis was carried out after charging the cell to 4.3 V (vs $Li^+$/Li) at 0.1 C, followed by resting for an hour to achieve an equilibrium state. The Nyquist plots were fitted using the EC-Lab software V11.10 with a combination Randomize+Simplex mode. This mode combines the Randomize mode, which calculates parameters yielding the lowest value of goodness-of-fit ($\chi^2$), with the Simplex mode as a minimization method, primarily used to minimize linear functions. Fitting was ceased manually after the weighted goodness-of-fit $\left(\frac{\chi^2}{|Z|}\right)$ reached an order of $10^{-2}$. In situ electronic resistance measurements were conducted under a 10 mV bias using a homemade cell. This cell consists of Li−In|LPSCl|$LiCoO_2$ configurations, where an aluminum mesh (approximately 60 $\mu$m) serving as the auxiliary electrode was embedded between the cathode composite layer and the LPSCl electrolyte layer. The working electrode consisted of 35 mg of composite cathode ($LiCoO_2$/LPSCl = 13:7 as a weight ratio). Operando electrochemical pressiometry measurements were conducted using a high-resolution pressure sensor with a sensitivity of 0.01 kg (load cell, BONGSHIN), and the baseline of the pressure change curves was subtracted using Origin software.

## 3. RESULTS AND DISCUSSION

**3.1. Electrochemical Performance: Bare $LiCoO_2$ vs Surface-Regulated $LiCoO_2$−$Li_2SnO_3$ Core−Shell Nanoparticles.** In order to clarify the role of LPSCl decomposition on the nanostructured cathode surface in the interfacial


https://doi.org/10.1021/acs.chemmater.4c00629
Chem. Mater. 2024, 36, 5215−5227

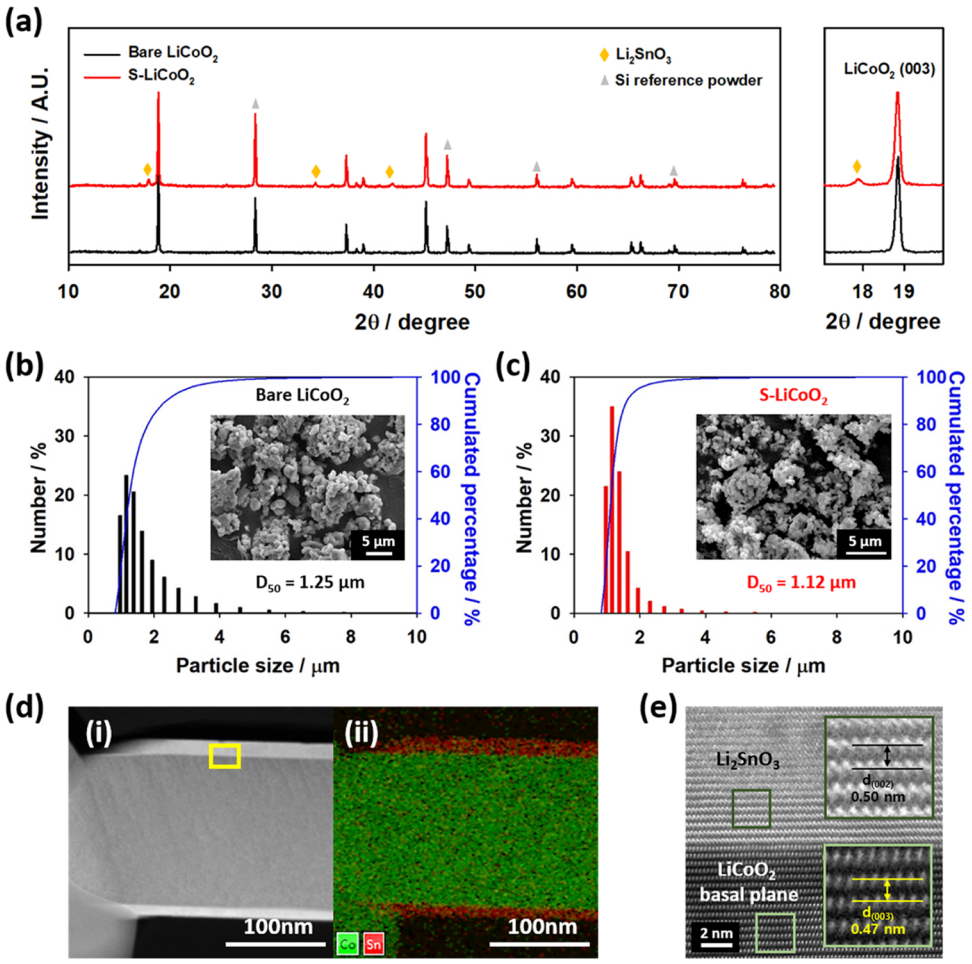


**Figure 1.** (a) XRD patterns of bare $LiCoO_2$ (black) and S-$LiCoO_2$ (red). The yellow diamond and gray triangle symbols marked in panel (a) correspond to $Li_2SnO_3$ and silicon reference powders, respectively. Particle size distribution for (b) bare $LiCoO_2$ and (c) S-$LiCoO_2$. Their insets show each corresponding SEM image of bare $LiCoO_2$ and S-$LiCoO_2$. (d) Cross-sectional (i) STEM and (ii) corresponding EDS mapping images of S-$LiCoO_2$. Green and red colors represent cobalt and tin elements, respectively. (e) Z-contrast HAADF image of the selected area of (i) in panel (d). Bright gray and dark gray domains correspond to $Li_2SnO_3$ and $LiCoO_2$, respectively. Their insets display the inverse-FFT images of each selected area in panel (e) to provide their *d*-spacing values for clarity.

degradation mode, specifically interfacial void formation, of the composite cathode electrode, we compared the electrochemical and chemical behaviors of bare and surface-regulated $LiCoO_2$ nanoparticles. Both types of $LiCoO_2$ nanoparticles were synthesized using a sol−gel method. In particular, surface-regulated $LiCoO_2$−$Li_2SnO_3$ core−shell nanoparticles (denoted as S-$LiCoO_2$) were obtained through plane-selective segregation synthesis.[37] This segregation method exploits the fact that the solubility of Sn in $LiCoO_2$ varies with the heating temperature. Figure 1a shows the XRD patterns of both bare $LiCoO_2$ and S-$LiCoO_2$ nanoparticles. Their XRD peaks appear at nearly identical $2\theta$ positions, implying that they have the almost same lattice parameters. This indicates that S-$LiCoO_2$ is not doped with Sn. Additionally, S-$LiCoO_2$ contains an additional phase of $\beta$-$Li_2SnO_3$, implying that S-$LiCoO_2$ consists of a mixed phase of $LiCoO_2$ and $\beta$-$Li_2SnO_3$.[37,38] The particle size distribution (PSD) of bare $LiCoO_2$ and S-$LiCoO_2$ nanoparticles, along with their corresponding SEM images (insets), is presented in Figure 1b,c, respectively. Both bare $LiCoO_2$ and S-$LiCoO_2$ exhibit a similar pebble-like morphology and are several hundred nanometers in size. They have comparable size distributions, with the average diameters ($D_{50}$) of bare $LiCoO_2$ and S-$LiCoO_2$ being approximately 1.25 and 1.12 $\mu$m, respectively. The size of the powders measured from PSD was larger than that observed in SEM, which is attributed to the agglomeration of nanoparticles. Figure 1d displays the cross-sectional scanning transmission electron microscopy (STEM) and corresponding EDS mapping images of S-$LiCoO_2$. Figure 1e further shows the Z-contrast high-angle annular dark-field (HAADF) image of S-$LiCoO_2$ at the interface between the Sn-rich and Co-rich regions, as indicated by the yellow box in Figure 1d. The *d*-spacing values along the *c*-axis in these two regions reveal that the phases of the Sn-rich and Co-rich regions correspond to $\beta$-$Li_2SnO_3$ and $LiCoO_2$, respectively.[39,40] The cross-sectional SEM/EDS mapping images of S-$LiCoO_2$ nanoparticles are also presented in Figure S1. This suggests that $\beta$-$Li_2SnO_3$ is uniformly coated on the $LiCoO_2$ surface. The SEM image and XRD pattern of LPSCl powders are displayed in Figure S2.

$Li_2SnO_3$, being electrochemically stable at high voltages, has been widely employed as a surface coating material to enhance the electrochemical performance of various cathode materials.[37,41−43] However, the chemical stability of $Li_2SnO_3$ in contact with LPSCl has not been extensively investigated. In this regard, $Li_2SnO_3$ powders were synthesized using a solid-state synthesis method.[44] Subsequently, each of $Li_2SnO_3$ and


https://doi.org/10.1021/acs.chemmater.4c00629
Chem. Mater. 2024, 36, 5215−5227

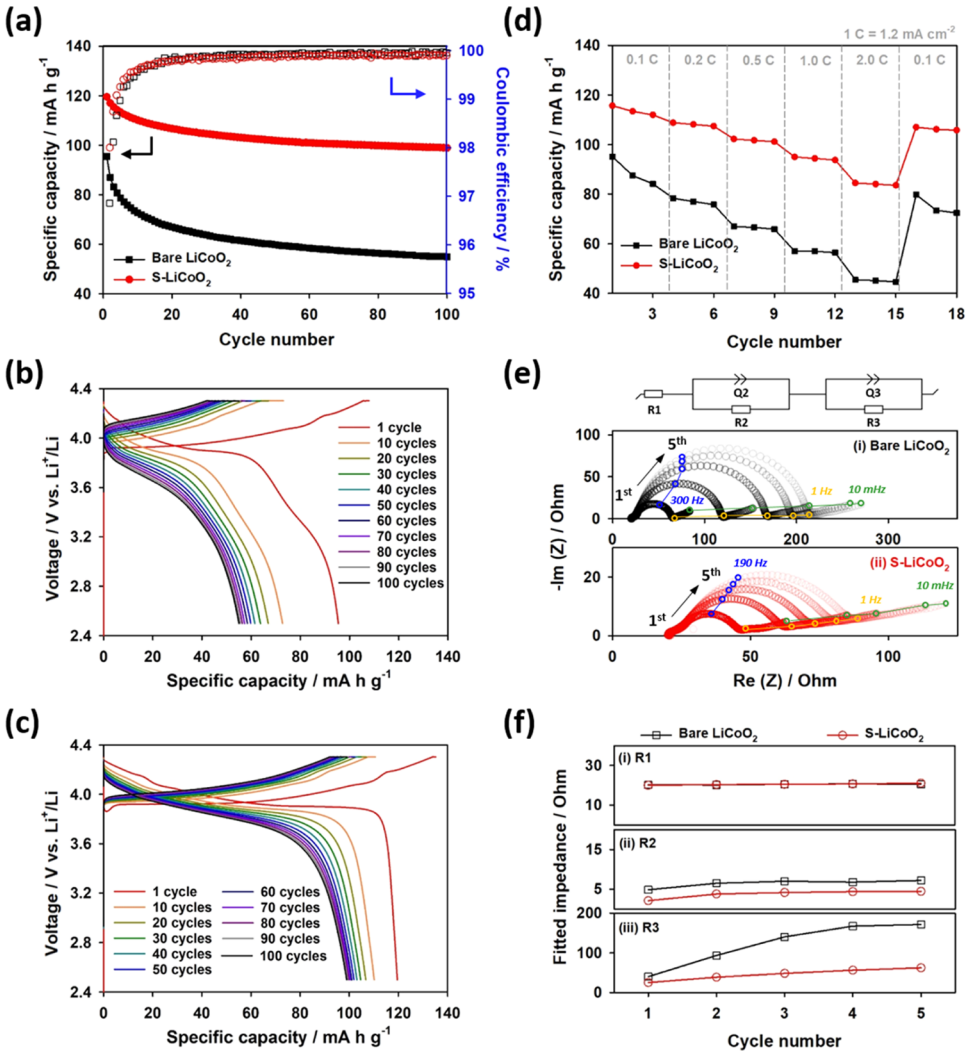


**Figure 2.** (a) Cycle performance (discharge capacity) and Coulombic efficiency of Li|LPSCl|$LiCoO_2$ cells for bare $LiCoO_2$ and S-$LiCoO_2$ at a current density of 0.1C (0.12 mA $cm^{-2}$) in the voltage range of 2.5−4.3 V (vs $Li^+$/Li). Voltage profiles of (b) bare $LiCoO_2$ and (c) S-$LiCoO_2$ for various cycle numbers. (d) Rate performance (discharge capacity) of bare $LiCoO_2$ and S-$LiCoO_2$ at various discharge current densities. (e) Nyquist plots and (f) corresponding fitting parameters of bare $LiCoO_2$ and S-$LiCoO_2$ for five cycles. Fitting was performed using the equivalent circuit model in panel (e).

bare $LiCoO_2$ powders was mixed and pelletized with LPSCl powders. The resulting mixture pellets were then stored under an Ar atmosphere at room temperature for 48 h. Figure S3a−d compares the XRD patterns and Raman spectra of $Li_2SnO_3$, $LiCoO_2$, and LPSCl and their mixture pellets after storage. The crystal structures of LPSCl remained almost unchanged during storage with both $Li_2SnO_3$ and $LiCoO_2$. This indicates that the bulk structure of LPSCl was not degraded upon contact with these materials. However, surface degradation of LPSCl varied depending on the type of mixing material. Figure S3e presents the XPS spectra of the S 2p peak for LPSCl powder and its mixed pellets with $Li_2SnO_3$ and $LiCoO_2$ after storage under an Ar atmosphere at room temperature for 48 h. When LPSCl was in contact with $Li_2SnO_3$, no significant side reactions were observed on the surface. In contrast, upon contact with $LiCoO_2$, numerous byproducts, such as $SO_3$, $SO_4$, and $P_2S_x$, were detected at the interface.[6,15,16] This suggests that $Li_2SnO_3$ suppresses the decomposition of LPSCl on the surface of S-$LiCoO_2$ compared to bare $LiCoO_2$.

We compared the electrochemical performance of bare $LiCoO_2$ and S-$LiCoO_2$ using a bulk-type cell, which consisted of a composite cathode pellet, a solid electrolyte pellet, and a Li metal foil anode. It is important to note that the composite cathode pellet was composed of $LiCoO_2$ and LPSCl powders without carbon additives. This electrode structure was deliberately designed to eliminate any potential contribution from LPSCl decomposition on the carbon additive surface to the electrochemical performance of $LiCoO_2$.[45,46] Figure 2a−c illustrates the cycle performance, Coulombic efficiency, and the corresponding voltage profiles of both bare $LiCoO_2$ and S-$LiCoO_2$ within the voltage range of 2.5−4.3 V (vs $Li^+$/Li). Due to the absence of carbon additives in the cathode electrodes, a low current density of 0.1C (0.12 mA $cm^{-2}$) was applied, attributed to the poor electrical conductivity of the composite cathode pellets.[47,48] The thickness of the composite electrode pellet, which contained no carbon additives, was approximately 45 $\mu$m, as shown in the cross-sectional SEM image (Figure S4). S-$LiCoO_2$ delivered a larger discharge capacity (119.6 mA h $g^{-1}$) in the initial cycle compared to bare $LiCoO_2$ (95.1 mA h $g^{-1}$). Additionally, S-$LiCoO_2$ demonstrated more stable capacity retention and a smaller overpotential over 100 cycles than bare $LiCoO_2$. The rate performance of S-$LiCoO_2$ was also


https://doi.org/10.1021/acs.chemmater.4c00629
Chem. Mater. 2024, 36, 5215−5227

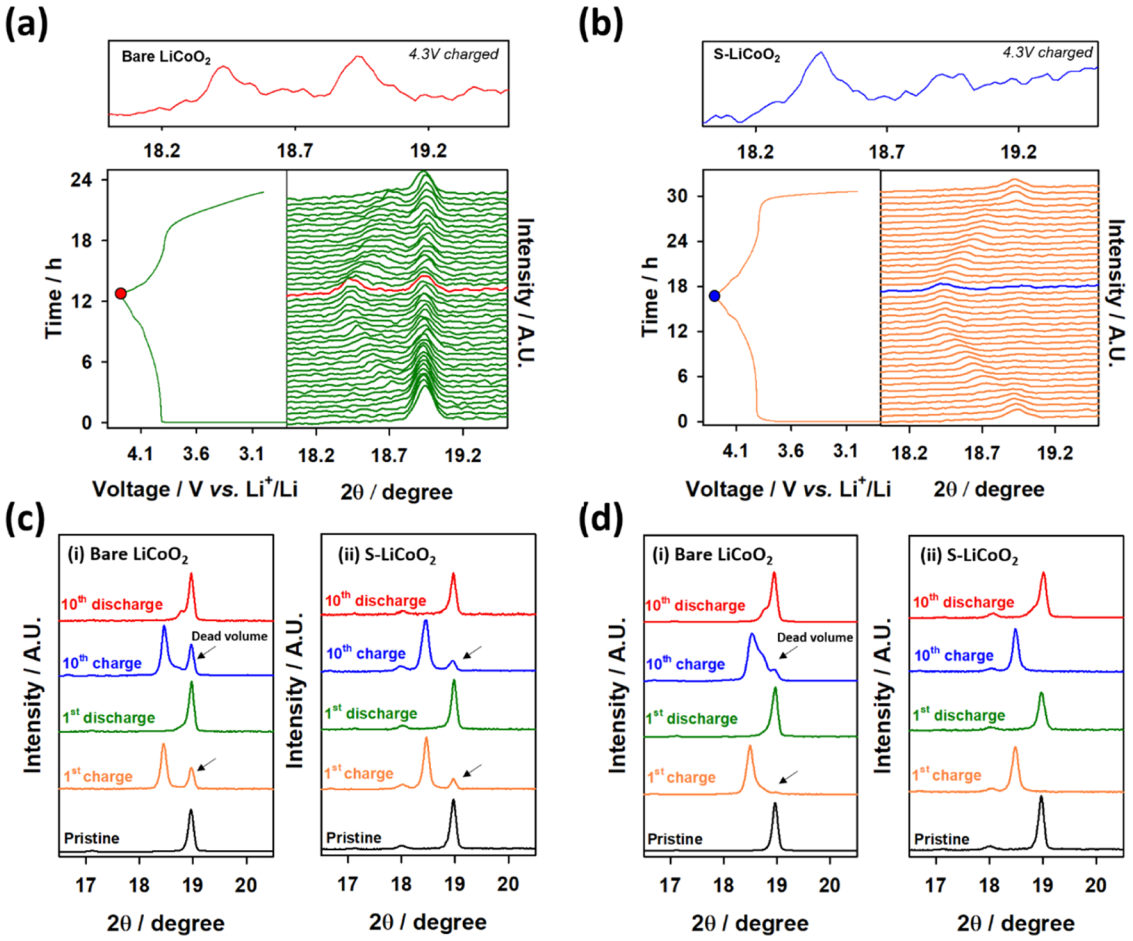


**Figure 3.** Initial voltage profiles and corresponding in situ XRD patterns in the selected 2$\theta$ range of 18.0−19.5° for (a) bare $LiCoO_2$ and (b) S-$LiCoO_2$. The XRD patterns of the fully charged state at 4.3 V (vs $Li^+$/Li) are magnified for clarity. Ex situ XRD patterns of the two distinct $LiCoO_2$ composite cathodes (c) without carbon additives and (d) with carbon additives in the selected 2$\theta$ range of 16.5−20.5° for (i) bare $LiCoO_2$ and (ii) S-$LiCoO_2$. The electrodes were retrieved after the first and tenth cycles.

superior to that of bare $LiCoO_2$, as shown in Figure 2d. This improvement is attributed to the fact that the charge-transfer resistance of bare $LiCoO_2$ was significantly larger than that of S-$LiCoO_2$, as demonstrated by the comparative EIS analysis. Figures 2e and S5 display the Nyquist and Bode plots of bare $LiCoO_2$ and S-$LiCoO_2$ during the initial five cycles. The spectra were fitted within selected ranges to observe the instability of the $LiCoO_2$/LPSCl interface, utilizing the equivalent circuit model in Figure 2e.[13,45,49] The fitted spectra of bare $LiCoO_2$ and S-$LiCoO_2$ electrodes are shown in Figures S6a and 6b, respectively. $R_1$, $R_2$, and $R_3$ in the circuit represent the resistance of the solid electrolyte, grain boundary resistance of the solid electrolyte, and interfacial resistance between the cathode material and the solid electrolyte, respectively. The changes in the three resistances of bare $LiCoO_2$ and S-$LiCoO_2$ during the initial five cycles are presented in Figure 2f. The values of all fitting parameters, including resistances ($R_1$, $R_2$, and $R_3$) and capacitances ($Q_2$ and $Q_3$), are displayed in Table S1. These results indicate that the charge-transfer resistance ($R_3$) of bare $LiCoO_2$ was significantly larger than that of S-$LiCoO_2$ and, further, that bare $LiCoO_2$ exhibited a more pronounced increase in charge-transfer resistance during cycling compared to S-$LiCoO_2$.

**3.2. Capacity Decay of $LiCoO_2$ Nanoparticles due to the Formation of Dead Particles.** To investigate the failure mode of nanostructured $LiCoO_2$, we performed both in situ and ex situ XRD analyses.[7,9,17] Figure 3a,b presents the in situ XRD patterns of bare $LiCoO_2$ and S-$LiCoO_2$, respectively, during the initial cycle within the selected 2$\theta$ range of 18.0−19.5°. The magnified XRD patterns of the fully charged state at 4.3 V (vs $Li^+$/Li) were included for clarity. Note that the in situ XRD cell operated at a low pressure of approximately 1 MPa, whereas the electrochemical performance of the bulk-type cell was evaluated at a higher pressure of approximately 50 MPa. The in situ XRD cell was charged and discharged at a 0.05C. The composite cathode pellets used for the in situ XRD analysis consisted of $LiCoO_2$ and LPSCl powders without carbon additives, ensuring that the in situ cell operated under the same conditions as those used for evaluating the electrochemical performance. In the case of S-$LiCoO_2$, the (003) peak of the fully lithiated phase at approximately 19° gradually shifted to a lower 2$\theta$ during charging and reversibly shifted to a higher 2$\theta$ during the subsequent discharge, as shown in Figure 3b. This (003) peak of the fully lithiated phase at approximately 19° almost completely disappeared at 4.3 V (vs $Li^+$/Li), implying that nearly all S-$LiCoO_2$ nanoparticles were delithiated during charging. However, for bare $LiCoO_2$, two distinct (003) peaks were observed even after full charging, as depicted in Figure 3a. The two (003) peaks at approximately 18.5 and 19° correspond to the fully delithiated and fully lithiated phases of $LiCoO_2$, respectively. Specifically, the partial (003) peak of bare $LiCoO_2$ shifted reversibly during


https://doi.org/10.1021/acs.chemmater.4c00629
Chem. Mater. 2024, 36, 5215−5227

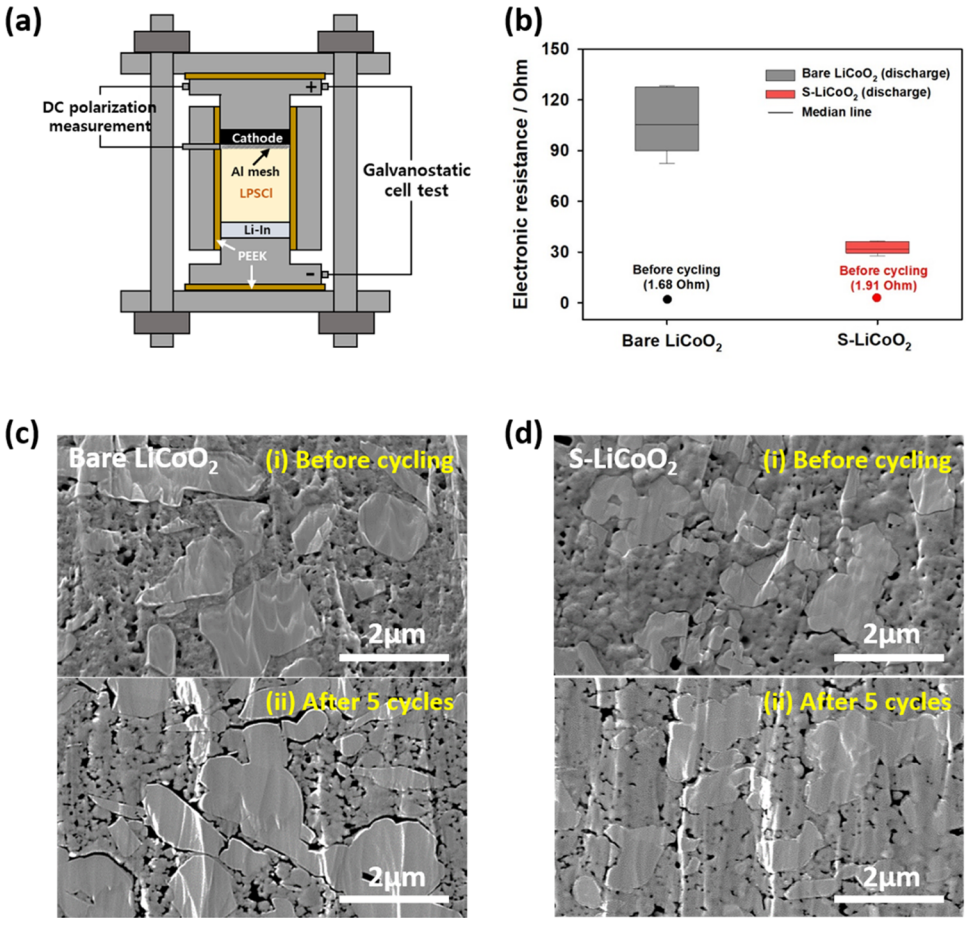


**Figure 4.** (a) Schematic illustration of the homemade cell used for in situ electronic resistance measurement of the composite cathode electrode during cycling. (b) Average electronic resistance of the composite cathode electrode of bare $LiCoO_2$ and S-$LiCoO_2$ at the fully discharged state over the initial five cycles. The electronic resistances of the pristine electrodes (denoted as "before cycling") are marked as filled circles. Cross-sectional SEM images of (c) bare $LiCoO_2$ and (d) S-$LiCoO_2$ (i) before cycling and (ii) after five cycles.

charging and discharging, similar to that of S-$LiCoO_2$. However, the (003) peak of the fully lithiated phase at approximately 19° did not disappear completely and remained weakly present without a peak shift during charging. This indicates that some of the bare $LiCoO_2$ nanoparticles in the composite cathode were not delithiated during charging, leading to the formation of electrochemically inactive "dead particles" due to contact loss.

The same "dead particles" behavior of $LiCoO_2$, attributed to contact loss, was observed in the ex situ XRD patterns of both bare $LiCoO_2$ and S-$LiCoO_2$ during cycling. For the ex situ XRD analysis, the bulk-type cells were disassembled after various cycle numbers, and the composite cathode pellets were retrieved. Two distinct types of composite cathode pellets were prepared for ex situ XRD analysis, consisting of $LiCoO_2$ and LPSCl powders: (i) without and (ii) with carbon additives. Figure 3c compares the ex situ XRD patterns of bare $LiCoO_2$ and S-$LiCoO_2$ without carbon additives in the composite cathode for various cycle numbers. After the initial full charge (4.3 V vs $Li^+/Li$) of bare $LiCoO_2$, two (003) peaks were observed at approximately 18.5 and 19°, corresponding to the fully delithiated and fully lithiated phases of $LiCoO_2$, respectively. This observation is consistent with the results from the in situ XRD analysis. The (003) peak of the fully lithiated phase remained intense even after the initial full charge (4.3 V vs $Li^+/Li$). Moreover, the intensity of this (003) peak of the fully lithiated phase at the fully charged state (4.3 V vs $Li^+/Li$) gradually increased during cycling, suggesting that the dead volume of the fully lithiated phase increased gradually during cycling. In contrast, the (003) peak of the fully lithiated phase in S-$LiCoO_2$ remained weak at the fully charged state (4.3 V vs $Li^+/Li$) and showed almost no change during cycling. This indicates that S-$LiCoO_2$ effectively suppressed the formation of dead volume driven by contact loss compared to bare $LiCoO_2$. Additionally, the evolution of dead volume in bare $LiCoO_2$ during cycling occurred irrespective of the addition of carbon additives in the composite cathode, as demonstrated in Figure 3d. We examined a composite cathode pellet consisting of $LiCoO_2$ nanoparticles, LPSCl, and Super P in a weight ratio of 12:7:1, respectively. Figure S7 shows the cycle performance and corresponding voltage profiles of the bare $LiCoO_2$ and S-$LiCoO_2$ composite pellets containing carbon additives.

To demonstrate the origin of dead volume formation in bare $LiCoO_2$ during cycling, we performed in situ electronic conductivity measurements on a composite cathode pellet containing no carbon additives.[50] The schematic diagram of the in situ electronic resistance measurement cell is presented in Figure 4a. An Al mesh, serving as auxiliary electrode, was placed between the composite cathode and the LPSCl electrolyte pellets. Figure S8 shows the voltage profiles of bare $LiCoO_2$ and S-$LiCoO_2$ for these cells. DC polarization


https://doi.org/10.1021/acs.chemmater.4c00629
Chem. Mater. 2024, 36, 5215−5227

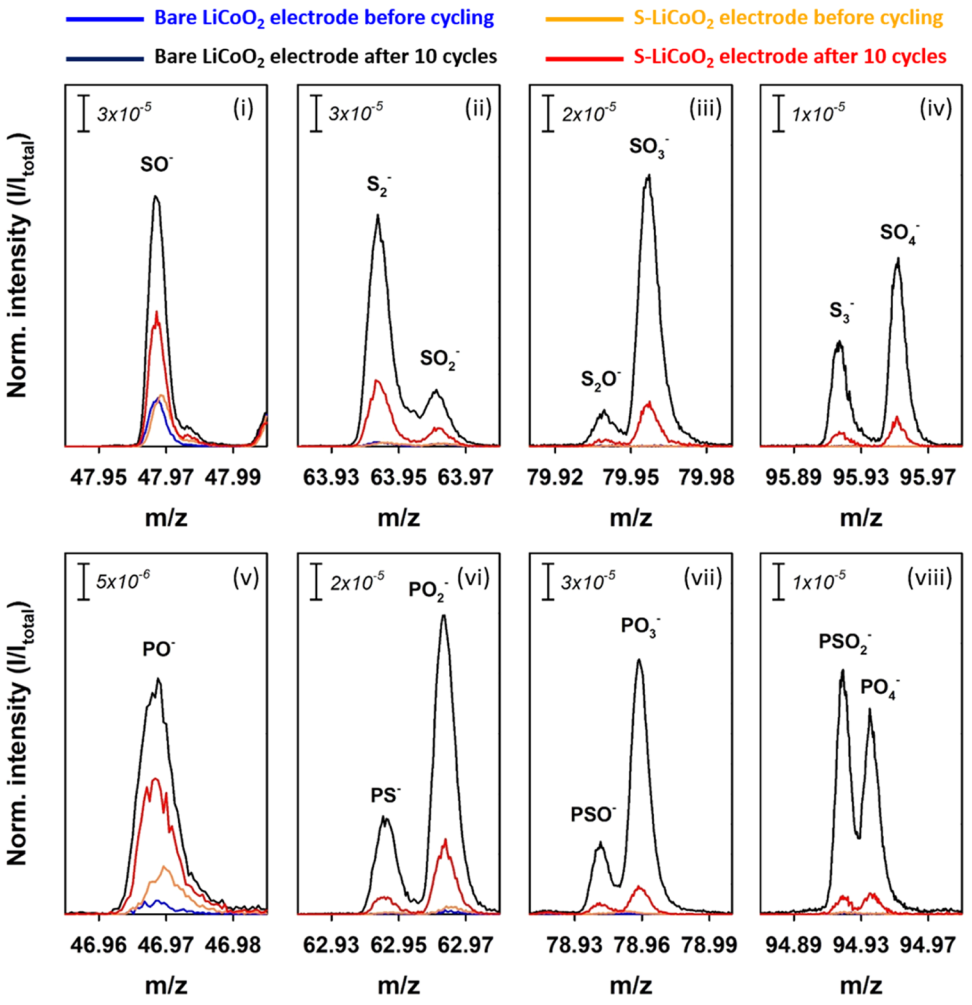


**Figure 5.** Normalized TOF-SIMS spectra of bare $LiCoO_2$ and S-$LiCoO_2$ for various fragments: (i–iv) Sulfur oxide ($SO_x^-$), (v–viii) phosphorus oxide ($PO_y^-$), and (ii, iv) polysulfide ($S_z^-$). The blue, black, orange, and red spectra represent pristine bare $LiCoO_2$ electrode (before cycling), bare $LiCoO_2$ electrode after 10 cycles, pristine S-$LiCoO_2$ electrode (before cycling), and S-$LiCoO_2$ electrode after 10 cycles, respectively. Scale bars of normalized intensity for various fragments are inserted in each figure.

was measured between the Al mesh and the current collector of the composite cathode after each full discharge during five cycles, as shown in Figure S9. Figure 4b shows the average electronic resistance of the composite cathode pellet at the fully discharged state over five cycles. We observed changes in the electronic resistance of the cathode pellet before and after cycling. Initially, the electronic resistance of the bare $LiCoO_2$ cathode pellet was similar to that of the S-$LiCoO_2$ cathode pellet. However, after cycling, the bare $LiCoO_2$ cathode pellet exhibited a significant increase in electronic resistance compared to the S-$LiCoO_2$ cathode pellet. The larger increase in bare $LiCoO_2$ is attributed to the formation of interfacial voids within the bare $LiCoO_2$ cathode pellet during cycling.[51] Figure 4c compares the cross-sectional SEM images of the bare $LiCoO_2$ cathode pellet before and after cycling. Before cycling, the SEM image shows intimate contact between $LiCoO_2$ and LPSCl particles, with negligible voids at their interfaces. However, significant void formation at the interface between $LiCoO_2$ and LPSCl particles was observed after cycling. In contrast, the cross-sectional SEM images of the S-$LiCoO_2$ cathode pellet showed negligible changes before and after cycling, as depicted in Figure 4d. The minimal void formation in S-$LiCoO_2$ during cycling implies that S-$LiCoO_2$ effectively suppressed interfacial void formation. This suggests that the formation of dead volume in bare $LiCoO_2$ during cycling was due to contact loss resulting from interfacial void formation.

The interfacial void formation in bare $LiCoO_2$ during cycling was more significant compared to that in S-$LiCoO_2$. Interfacial voids can form through two distinct mechanisms: (i) the volume change of $LiCoO_2$ between charging and discharging and (ii) oxidative electrolyte decomposition of LPSCl, as discussed in Section 1. Since bare $LiCoO_2$ exhibited a smaller reversible capacity during cycling than S-$LiCoO_2$, as shown in Figure 2a, the volume change of bare $LiCoO_2$ between charging and discharging was definitely less pronounced than that of S-$LiCoO_2$. This will be further discussed later in the section on operando electrochemical pressiometry analysis. This indicates that the significant interfacial void formation in bare $LiCoO_2$, compared to S-$LiCoO_2$, was primarily due to the oxidative electrolyte decomposition of LPSCl during charging rather than the volume change of $LiCoO_2$ during cycling.

**3.3. Interfacial Void Formation Driven by Oxidative Decomposition of Electrolytes.** Figure 5 compares the ex situ TOF-SIMS spectra of bare $LiCoO_2$ and S-$LiCoO_2$ before and after cycling. The relative amounts of decomposed species of LPSCl were estimated from the normalized peak intensities of each species, where the intensity of each fragment was divided by the total intensity of all fragments.[6,12,52] Before


https://doi.org/10.1021/acs.chemmater.4c00629
Chem. Mater. 2024, 36, 5215–5227

cycling, both bare $LiCoO_2$ and S-$LiCoO_2$ showed negligible amounts of oxygen-containing compounds, such as $SO_x^-$ and $PO_y^-$ (with $1 \leq x \leq 4$ and $1 \leq y \leq 4$) fragments. However, the intensities of these oxidized fragments increased significantly after cycling. In particular, the signal intensities of the oxidized fragments for bare $LiCoO_2$ were much more intense than those for S-$LiCoO_2$. This indicates that LPSCl underwent more extensive oxidation on the bare $LiCoO_2$ surface compared to the S-$LiCoO_2$ surface. A similar behavior was also observed for $S_z^-$ (with $2 \leq z \leq 3$) fragments. Consequently, the interfacial void formation driven by the oxidative decomposition of LPSCl was more pronounced in bare $LiCoO_2$. An oxidized LPSCl surface is known to exhibit greater brittleness and a higher Young's modulus compared to pristine LPSCl.[29] These degraded interfacial properties can accelerate the deterioration of intimate contact between LPSCl and $LiCoO_2$, particularly when combined with the volume changes of $LiCoO_2$ during cycling.

The formation of interfacial voids driven by the oxidative decomposition of LPSCl was further supported by GITT analysis. Figure 6a,b compares the GITT profiles and

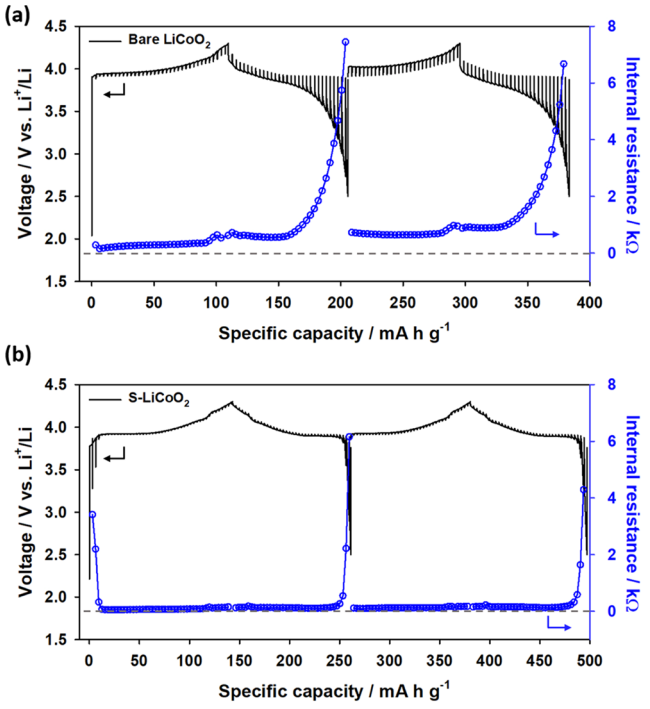


**Figure 6.** GITT profiles (black) and corresponding internal resistances (blue) of (a) bare $LiCoO_2$ and (b) S-$LiCoO_2$ during the initial two cycles.

corresponding internal resistances of bare $LiCoO_2$ and S-$LiCoO_2$ during the initial two cycles, respectively. The internal resistance was calculated by dividing the difference between the closed-circuit voltage and the quasi-open-circuit voltage by the applied current.[9,53] As shown in Figure 6a, the internal resistance of bare $LiCoO_2$ began to increase toward the end of the initial charge, and this increase became more pronounced in the subsequent cycles. This suggests that the oxidative decomposition of LPSCl on the bare $LiCoO_2$ surface contributed to the formation of interfacial voids, leading to a large overpotential due to poor electronic and ionic contacts. In contrast, S-$LiCoO_2$ exhibited negligible changes in internal resistance during the initial two cycles, as shown in Figure 6b. Furthermore, the internal resistance of S-$LiCoO_2$ was significantly lower than that of bare $LiCoO_2$, indicating that S-$LiCoO_2$ effectively suppressed the oxidative decomposition of LPSCl, consequently leading to minimal void formation at the interface.

Moreover, we conducted operando electrochemical pressiometry analysis to clarify the correlation between interfacial void formation and the decomposition of LPSCl, as illustrated in Figure 7.[22,54,55] Changes in the pressure of the bulk-type cell were monitored during cycling using a high-resolution pressure sensor (load cell) with a sensitivity of 0.01 kg (ca. 739 Pa). Instead of Li metal, $Li_4Ti_5O_{12}$ was employed as the anode. Given that $Li_4Ti_5O_{12}$ is a zero-strain material, experiencing no volume change during charging and discharging, any pressure variation in the cell during cycling can be attributed solely to the volume change of the $LiCoO_2$ composite cathode.[56] The SEM image and XRD pattern of $Li_4Ti_5O_{12}$ powders are presented in Figure S10. Figure 7a–c shows the voltage profiles and corresponding pressure change curves for three distinct cell configurations: $Li_4Ti_5O_{12}$|LPSCl|bare $LiCoO_2$/LPSCl, $Li_4Ti_5O_{12}$|LPSCl|S-$LiCoO_2$/LPSCl, and $Li_4Ti_5O_{12}$|LPSCl|bare $LiCoO_2$/$Li_3YCl_6$ (LYC). All cells contained equal amounts of active materials and maintained the same weight ratio of active material to solid electrolyte. Both the bare $LiCoO_2$/LPSCl and S-$LiCoO_2$/LPSCl cathodes exhibited a rapid pressure decay at the beginning of charging, occurring in the voltage range of 0.95–2.35 V (corresponding to 2.5–3.9 V vs $Li^+$/Li). In contrast, no such pressure decay was observed at the beginning of charging for the bare $LiCoO_2$/LYC cathode. This behavior is attributed to the fact that LYC was not decomposed on the $LiCoO_2$ surface during charging, as it is known to be electrochemically and chemically stable with $LiCoO_2$ in the voltage range of 2.5–4.3 V (vs $Li^+$/Li).[27,57,58] Figure S11 shows the SEM image and XRD pattern of LYC powders. In contrast, LPSCl underwent oxidative decomposition on the $LiCoO_2$ surface during charging, leading to the volume shrinkage of LPSCl.[17] Consequently, the pressure of the cell decreased at the beginning of charging in the $LiCoO_2$/LPSCl composite. The pressure decay in bare $LiCoO_2$ ($0.21 \times 10^5$ Pa) was more pronounced than that in S-$LiCoO_2$ ($0.14 \times 10^5$ Pa). This difference was due to the suppressed decomposition of LPSCl on the S-$LiCoO_2$ surface compared to the bare $LiCoO_2$ surface. Figure 7d compares the pressure changes over five cycles in terms of normalized time. Time was normalized for each configuration by dividing it by the respective total cycling period. The oscillating pressure changes during cycling were considered due to the variations in the lattice parameters of $LiCoO_2$ during charging and discharging.[59] S-$LiCoO_2$/LPSCl showed a slightly larger pressure change between charging and discharging compared to bare $LiCoO_2$/LPSCl. This implies that the volumetric change of S-$LiCoO_2$ was greater than that of bare $LiCoO_2$, attributed to its higher reversible capacity. These results suggest that the oxidative decomposition of LPSCl critically contributes to interfacial void formation of nanostructured $LiCoO_2$ during cycling, leading to poor electrochemical performance due to electronic and ionic contact loss.

## 4. CONCLUSIONS

During cycling, progressive degradation at the interface between oxide cathode materials and LPSCl, particularly due to the creation of interfacial voids, increased charge-transfer


https://doi.org/10.1021/acs.chemmater.4c00629
Chem. Mater. 2024, 36, 5215–5227

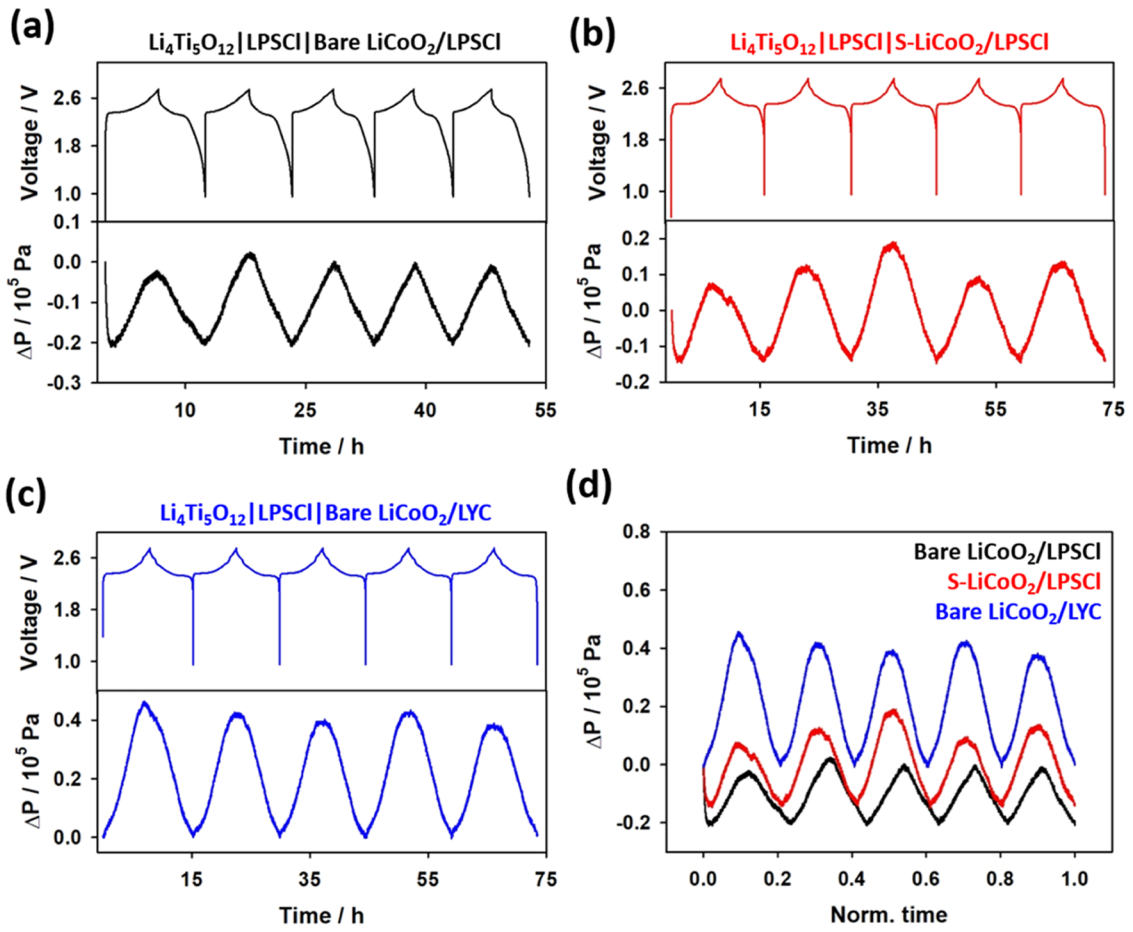


**Figure 7.** Voltage profiles and corresponding pressure change curves of (a) $Li_4Ti_5O_{12}$|LPSCl|bare $LiCoO_2$/LPSCl, (b) $Li_4Ti_5O_{12}$|LPSCl|S-$LiCoO_2$/LPSCl, and (c) $Li_4Ti_5O_{12}$|LPSCl|bare $LiCoO_2$/LYC cells over five cycles. (d) Comparative pressure change curves of three distinct cells in panels (a–c) as a function of normalized time. Time was normalized for each configuration by dividing it by the respective total cycling period.

resistance and eventually led to poor capacity retention. The presence of interfacial voids interrupted the intimate contact between LPSCl and oxide cathode particles, significantly affecting the electrochemical performance of ASSBs. The development of interfacial voids is driven by two distinct routes: (i) the volume change of oxide cathode materials during cycling and (ii) the volume shrinkage of LPSCl due to oxidative decomposition. However, the precise impact of each mechanism on the formation of interfacial voids remained ambiguous in previous literature, especially for nanostructured cathode materials. To address this, we compared the interfacial degradation behaviors of bare $LiCoO_2$ and surface-regulated $LiCoO_2$–$Li_2SnO_3$ core–shell nanoparticles. This comparison aimed to clarify the significant role of LPSCl's oxidative decomposition on the nanostructured $LiCoO_2$ surface in interfacial void formation during cycling, as compared to the volume change of $LiCoO_2$ between charging and discharging. We investigated their degradation behaviors using various advanced analytical techniques, including in situ XRD, in situ electronic resistance measurement, and operando electrochemical pressiometry.

Both bare $LiCoO_2$ and $LiCoO_2$–$Li_2SnO_3$ exhibited similar particle size distributions and reversible capacities, undergoing comparable absolute volume changes between charging and discharging. This was supported by operando electrochemical pressiometry. This similarity allowed us to rule out the potential impact of $LiCoO_2$'s volume change during cycling on the formation of interfacial voids. Notably, $LiCoO_2$–$Li_2SnO_3$ showed mitigated formation of interfacial voids during cycling, compared to bare $LiCoO_2$. This reduction in void formation led to a decrease in the creation of electrochemically inactive "dead volume" within the $LiCoO_2$–$Li_2SnO_3$ composite cathode during cycling, resulting in improved electrochemical performance compared to bare $LiCoO_2$. This is attributed to the fact that $LiCoO_2$–$Li_2SnO_3$ suppressed the oxidative decomposition of LPSCl during charging due to the enhanced chemical stability of $Li_2SnO_3$ with LPSCl. Consequently, this revealed that the oxidative decomposition of LPSCl on the nanostructured $LiCoO_2$ surface contributed more significantly to interfacial void formation during cycling than the volume change of $LiCoO_2$ itself. Our findings suggest that the oxidative decomposition of LPSCl is a predominant factor of nanostructured $LiCoO_2$ in the formation of interfacial voids, leading to poor electrochemical performance due to the loss of electronic and ionic contact.

## ■ ASSOCIATED CONTENT

### Supporting Information

The Supporting Information is available free of charge at https://pubs.acs.org/doi/10.1021/acs.chemmater.4c00629.

Cross-sectional SEM and corresponding EDS mapping images of $LiCoO_2$–$Li_2SnO_3$ core–shell nanoparticles; SEM image and XRD pattern of commercial LPSCl; XRD patterns, Raman, and XPS spectra of materials;



https://doi.org/10.1021/acs.chemmater.4c00629
Chem. Mater. 2024, 36, 5215–5227

cross-sectional SEM image of composite cathode pellet; Bode and Nyquist plots and corresponding fitted spectra; cycle performance and corresponding voltage profiles; voltage profiles of Li−In|LPSCl|Al mesh|LPSCl/$LiCoO_2$ cell; chronoamperometry profiles of composite cathode pellet; and SEM images and XRD patterns of $Li_4Ti_5O_{12}$ and LYC (PDF)

## AUTHOR INFORMATION


### Corresponding Authors

**Yoon Seok Jung** − *Department of Chemical and Biomolecular Engineering, Yonsei University, Seoul 03722, Republic of Korea;* orcid.org/0000-0003-0357-9508; Email: yoonsjung@yonsei.ac.kr

**Kyu Tae Lee** − *School of Chemical and Biological Engineering, Institute of Chemical Processes, Institute of Engineering Research, Seoul National University, Seoul 08826, Republic of Korea;* orcid.org/0000-0003-2769-3372; Email: ktlee@snu.ac.kr

### Authors

**Kanghyeon Kim** − *School of Chemical and Biological Engineering, Institute of Chemical Processes, Institute of Engineering Research, Seoul National University, Seoul 08826, Republic of Korea*

**Seunggoo Jun** − *Department of Chemical and Biomolecular Engineering, Yonsei University, Seoul 03722, Republic of Korea*

**Taehun Kim** − *School of Chemical and Biological Engineering, Institute of Chemical Processes, Institute of Engineering Research, Seoul National University, Seoul 08826, Republic of Korea*

**Jong Seok Kim** − *Department of Chemical and Biomolecular Engineering, Yonsei University, Seoul 03722, Republic of Korea*

**Seonghyun Lee** − *School of Chemical and Biological Engineering, Institute of Chemical Processes, Institute of Engineering Research, Seoul National University, Seoul 08826, Republic of Korea*

**Gawon Song** − *School of Chemical and Biological Engineering, Institute of Chemical Processes, Institute of Engineering Research, Seoul National University, Seoul 08826, Republic of Korea*

**Junsung Park** − *School of Chemical and Biological Engineering, Institute of Chemical Processes, Institute of Engineering Research, Seoul National University, Seoul 08826, Republic of Korea*

Complete contact information is available at: https://pubs.acs.org/10.1021/acs.chemmater.4c00629


### Author Contributions

[§]K.K. and S.J. contributed equally to this work. All of the authors have given approval to the final version of the manuscript.

### Notes

The authors declare no competing financial interest.

## ACKNOWLEDGMENTS

This work was supported by the National Research Foundation of Korea (NRF) grant funded by the Korean Government (MSIT) (No. RS-2023-00261543) and the Technology Innovation Program (20024818, Development of High-Strength Corrosion Resistant Lightweight Current Collector Material Technology for Sulfide-Based All-Solid-State Batteries) funded by the Ministry of Trade, Industry & Energy (MOTIE, Korea).

## REFERENCES


(1) Janek, J.; Zeier, W. G. Challenges in Speeding Up Solid-State Battery Development. *Nat. Energy* **2023**, *8*, 230−240.

(2) Duchêne, L.; Remhof, A.; Hagemann, H.; Battaglia, C. Status and Prospects of Hydroborate Electrolytes for All-Solid-State Batteries. *Energy Storage Mater.* **2020**, *25*, 782−794.

(3) Lee, Y.; Jeong, J.; Lee, H. J.; Kim, M.; Han, D.; Kim, H.; Yuk, J. M.; Nam, K.-W.; Chung, K. Y.; Jung, H.-G.; Yu, S. Lithium Argyrodite Sulfide Electrolytes with High Ionic Conductivity and Air Stability for All-Solid-State Li-Ion Batteries. *ACS Energy Lett.* **2022**, *7* (1), 171−179.

(4) Hennequart, B.; Deschamps, M.; Chometon, R.; Leube, B.; Dugas, R.; Quemin, E.; Cabelguen, P.-E.; Lethien, C.; Tarascon, J.-M. Solid-Electrolyte-Free O3-$Li_xTiS_2$ Cathode for High-Energy-Density All-Solid-State Lithium-Metal Batteries. *ACS Appl. Energy Mater.* **2023**, *6*, 8521−8531.

(5) Zhu, Y.; Mo, Y. Materials Design Principles for Air-Stable Lithium/Sodium Solid Electrolytes. *Angew. Chem., Int. Ed.* **2020**, *59*, 17472−17476.

(6) Kim, K.; Kim, T.; Song, G.; Lee, S.; Jung, M. S.; Ha, S.; Ha, A. R.; Lee, K. T. Trimethylsilyl Compounds for the Interfacial Stabilization of Thiophosphate-Based Solid Electrolytes in All-Solid-State Batteries. *Adv. Sci.* **2023**, *10*, No. 2303308.

(7) Kim, J. S.; Jung, S.; Kwak, H.; Han, Y.; Kim, S.; Lim, J.; Lee, Y. M.; Jung, Y. S. Synergistic Halide-Sulfide Hybrid Solid Electrolytes for Ni-Rich Cathodes Design Guided by Digital Twin for All-Solid-State Li Batteries. *Energy Storage Mater.* **2023**, *55*, 193−204.

(8) Tan, D. H. S.; Wu, E. A.; Nguyen, H.; Chen, Z.; Marple, M. A.; Doux, J.-M.; Wang, X.; Yang, H.; Banerjee, A.; Meng, Y. S. Elucidating Reversible Electrochemical Redox of $Li_6PS_5Cl$ Solid Electrolyte. *ACS Energy Lett.* **2019**, *4*, 2418−2427.

(9) Kim, J.; Lee, W.; Seok, J.; Lee, E.; Choi, W.; Park, H.; Yun, S.; Kim, M.; Lim, J.; Yoon, W.-S. Inhomogeneous Lithium-Storage Reaction Triggering the Inefficiency of All-Solid-State Batteries. *J. Energy Chem.* **2022**, *66*, 226−236.

(10) Zahiri, B.; Patra, A.; Kiggins, C.; Yong, A. X. B.; Ertekin, E.; Cook, J. B.; Braun, P. V. Revealing the Role of the Cathode−Electrolyte Interface on Solid-State Batteries. *Nat. Mater.* **2021**, *20*, 1392−1400.

(11) Nishio, K.; Imazeki, D.; Kurushima, K.; Takeda, Y.; Edamura, K.; Nakayama, R.; Shimizu, R.; Hitosugi, T. Immense Reduction in Interfacial Resistance between Sulfide Electrolyte and Positive Electrode. *ACS Appl. Mater. Interfaces* **2022**, *14*, 34620−34626.

(12) Walther, F.; Koerver, R.; Fuchs, T.; Ohno, S.; Sann, J.; Rohnke, M.; Zeier, W. G.; Janek, J. Visualization of the Interfacial Decomposition of Composite Cathodes in Argyrodite-Based All-Solid-State Batteries Using Time-of-Flight Secondary-Ion Mass Spectrometry. *Chem. Mater.* **2019**, *31*, 3745−3755.

(13) Koerver, R.; Aygün, I.; Leichtweiß, T.; Dietrich, C.; Zhang, W.; Binder, J. O.; Hartmann, P.; Zeier, W. G.; Janek, J. Capacity Fade in Solid-State Batteries: Interphase Formation and Chemomechanical Processes in Nickel-Rich Layered Oxide Cathodes and Lithium Thiophosphate Solid Electrolytes. *Chem. Mater.* **2017**, *29*, 5574−5582.

(14) Zhu, Y.; He, X.; Mo, Y. Origin of Outstanding Stability in the Lithium Solid Electrolyte Materials: Insights from Thermodynamic Analyses Based on First-Principles Calculations. *ACS Appl. Mater. Interfaces* **2015**, *7*, 23685−23693.

(15) Auvergniot, J.; Cassel, A.; Ledeuil, J.-B.; Viallet, V.; Seznec, V.; Dedryvère, R. Interface Stability of Argyrodite $Li_6PS_5Cl$ toward $LiCoO_2$, $LiNi_{1/3}Co_{1/3}Mn_{1/3}O_2$, and $LiMn_2O_4$ in Bulk All-Solid-State Batteries. *Chem. Mater.* **2017**, *29*, 3883−3890.

(16) Wang, C.; Hwang, S.; Jiang, M.; Liang, J.; Sun, Y.; Adair, K.; Zheng, M.; Mukherjee, S.; Li, X.; Li, R.; et al. Deciphering Interfacial Chemical and Electrochemical Reactions of Sulfide-Based All-Solid-State Batteries. *Adv. Energy Mater.* **2021**, *11*, No. 2100210.
(17) Han, Y.; Jung, S. H.; Kwak, H.; Jun, S.; Kwak, H. H.; Lee, J. H.; Hong, S. T.; Jung, Y. S. Single- or Poly-Crystalline Ni-Rich Layered Cathode, Sulfide or Halide Solid Electrolyte: Which Will be the Winners for All-Solid-State Batteries? *Adv. Energy Mater.* **2021**, *11*, No. 2100126.
(18) Wang, S.; Tang, M.; Zhang, Q.; Li, B.; Ohno, S.; Walther, F.; Pan, R.; Xu, X.; Xin, C.; Zhang, W.; Li, L.; Shen, Y.; Richter, F. H.; Janek, J.; Nan, C. W. Lithium Argyrodite as Solid Electrolyte and Cathode Precursor for Solid-State Batteries with Long Cycle Life. *Adv. Energy Mater.* **2021**, *11*, No. 2101370.
(19) Shi, T.; Zhang, Y.-Q.; Tu, Q.; Wang, Y.; Scott, M. C.; Ceder, G. Characterization of Mechanical Degradation in an All-Solid-State Battery Cathode. *J. Mater. Chem. A* **2020**, *8*, 17399−17404.
(20) Hlushkou, D.; Reising, A. E.; Kaiser, N.; Spannenberger, S.; Schlabach, S.; Kato, Y.; Roling, B.; Tallarek, U. The Influence of Void Space on Ion Transport in a Composite Cathode for All-Solid-State Batteries. *J. Power Sources* **2018**, *396*, 363−370.
(21) Reimers, J. N.; Dahn, J. R. Electrochemical and In Situ X-Ray Diffraction Studies of Lithium Intercalation in $Li_xCoO_2$. *J. Electrochem. Soc.* **1992**, *139*, No. 2091, DOI: 10.1149/1.2221184.
(22) Koerver, R.; Zhang, W.; de Biasi, L.; Schweidler, S.; Kondrakov, A. O.; Kolling, S.; Brezesinski, T.; Hartmann, P.; Zeier, W. G.; Janek, J. Chemo-Mechanical Expansion of Lithium Electrode Materials − on the Route to Mechanically Optimized All-Solid-State Batteries. *Energy Environ. Sci.* **2018**, *11*, 2142−2158.
(23) Kondrakov, A. O.; Schmidt, A.; Xu, J.; Geßwein, H.; Mönig, R.; Hartmann, P.; Sommer, H.; Brezesinski, T.; Janek, J. Anisotropic Lattice Strain and Mechanical Degradation of High- and Low-Nickel NCM Cathode Materials for Li-Ion Batteries. *J. Phys. Chem. C* **2017**, *121*, 3286−3294.
(24) Banerjee, A.; Wang, X.; Fang, C.; Wu, E. A.; Meng, Y. S. Interfaces and Interphases in All-Solid-State Batteries with Inorganic Solid Electrolytes. *Chem. Rev.* **2020**, *120*, 6878−6933.
(25) Conforto, G.; Ruess, R.; Schröder, D.; Trevisanello, E.; Fantin, R.; Richter, F. H.; Janek, J. Editors' Choice—Quantification of the Impact of Chemo-Mechanical Degradation on the Performance and Cycling Stability of NCM-Based Cathodes in Solid-State Li-Ion Batteries. *J. Electrochem. Soc.* **2021**, *168*, No. 070546.
(26) Yu, T.-Y.; Lee, H.-U.; Lee, J. W.; Park, S.-M.; Lee, I.-S.; Jung, H.-G.; Sun, Y.-K. Limitation of Ni-Rich Layered Cathodes in All-Solid-State Lithium Batteries. *J. Mater. Chem. A* **2023**, *11*, 24629−24636.
(27) Jang, J.; Chen, Y. T.; Deysher, G.; Cheng, D.; Ham, S. Y.; Cronk, A.; Ridley, P.; Yang, H.; Sayahpour, B.; Han, B.; Li, W.; Yao, W.; Wu, E. A.; Doux, J. M.; Nguyen, L. H. B.; Oh, J. A. S.; Tan, D. H. S.; Meng, Y. S. Enabling a Co-Free, High-Voltage $LiNi_{0.5}Mn_{1.5}O_4$ Cathode in All-Solid-State Batteries with a Halide Electrolyte. *ACS Energy Lett.* **2022**, *7*, 2531−2539.
(28) Zhou, Y.; Doerrer, C.; Kasemchainan, J.; Bruce, P. G.; Pasta, M.; Hardwick, L. J. Observation of Interfacial Degradation of $Li_6PS_5Cl$ against Lithium Metal and $LiCoO_2$ via In Situ Electrochemical Raman Microscopy. *Batteries Supercaps* **2020**, *3*, 647−652.
(29) Kato, A.; Nagao, M.; Sakuda, A.; Hayashi, A.; Tatsumisago, M. Evaluation of Young's Modulus of $Li_2S-P_2S_5-P_2O_5$ Oxysulfide Glass Solid Electrolytes. *J. Ceram. Soc. Jpn.* **2014**, *122*, 552−555.
(30) Sakuda, A.; Hayashi, A.; Tatsumisago, M. Sulfide Solid Electrolyte with Favorable Mechanical Property for All-Solid-State Lithium Battery. *Sci. Rep.* **2013**, *3*, No. 2261.
(31) Makishima, A.; Mackenzie, J. D. Direct Calculation of Young's Moidulus of Glass. *J. Non-Cryst. Solids* **1973**, *12*, 35−45.
(32) Doerrer, C.; Capone, I.; Narayanan, S.; Liu, J.; Grovenor, C. R. M.; Pasta, M.; Grant, P. S. High Energy Density Single-Crystal NMC/$Li_6PS_5Cl$ Cathodes for All-Solid-State Lithium-Metal Batteries. *ACS Appl. Mater. Interfaces* **2021**, *13*, 37809−37815.
(33) Payandeh, S.; Goonetilleke, D.; Bianchini, M.; Janek, J.; Brezesinski, T. Single versus Poly-Crystalline Layered Oxide Cathode Materials for Solid-State Battery Applications - A Short Review Article. *Curr. Opin. Electrochem.* **2022**, *31*, No. 100877.
(34) Zhao, W.; Zhang, Y.; Sun, N.; Liu, Q.; An, H.; Song, Y.; Deng, B.; Wang, J.; Yin, G.; Kong, F.; Lou, F.; Wang, J. Maintaining Interfacial Transports for Sulfide-Based All-Solid-State Batteries Operating at Low External Pressure. *ACS Energy Lett.* **2023**, *8*, 5050−5060.
(35) Liang, Z.; Xiao, Y.; Wang, K.; Jin, Y.; Pan, S.; Zhang, J.; Wu, Y.; Su, Y.; Zhong, H.; Yang, Y. Enabling Stable and High Areal Capacity Solid State Battery with Ni-Rich Cathode via Failure Mechanism Study. *Energy Storage Mater.* **2023**, *63*, No. 102987.
(36) Su, Y.; Liu, X.; Yan, H.; Zhao, J.; Cheng, Y.; Luo, Y.; Gu, J.; Zhong, H.; Fu, A.; Wang, K.; Wang, M.-S.; Huang, J.; Yan, J.; Yang, Y. Assembly of an Elastic & Sticky Interfacial Layer for Sulfide-Based All-Solid-State Batteries. *Nano Energy* **2023**, *113*, No. 108572.
(37) Kim, H.; Choi, G.; Kim, S.; Lee, D.; Doo, S. W.; Park, J.; Lee, W. B.; Lee, K. T. Plane-Selective Coating of $Li_2SnO_3$ on $Li[Ni_xCo_{1-x}]O_2$ for High Power Li ion Batteries. *J. Phys. Chem. Lett.* **2020**, *11*, 7096−7102.
(38) Wang, Q.; Huang, Y.; Miao, J.; Zhao, Y.; Wang, Y. Synthesis and Properties of Carbon-Doped $Li_2SnO_3$ Nanocomposite as Cathode Material for Lithium-Ion Batteries. *Mater. Lett.* **2012**, *71*, 66−69.
(39) Zhu, H.; Shen, R.; Tang, Y.; Yan, X.; Liu, J.; Song, L.; Fan, Z.; Zheng, S.; Chen, Z. Sn-Doping and $Li_2SnO_3$ Nano-Coating Layer Co-Modified $LiNi_{0.5}Co_{0.2}Mn_{0.3}O_2$ with Improved Cycle Stability at 4.6 V Cut-off Voltage. *Nanomaterials* **2020**, *10*, No. 868, DOI: 10.3390/nano10050868.
(40) Li, S.; Li, K.; Zheng, J.; Zhang, Q.; Wei, B.; Lu, X. Structural Distortion-Induced Charge Gradient Distribution of Co Ions in Delithiated $LiCoO_2$ Cathode. *J. Phys. Chem. Lett.* **2019**, *10*, 7537−7546.
(41) Li, Q.; Zhou, D.; Zhang, L.; Ning, D.; Chen, Z.; Xu, Z.; Gao, R.; Liu, X.; Xie, D.; Schumacher, G.; Liu, X. Tuning Anionic Redox Activity and Reversibility for a High-Capacity Li-Rich Mn-Based Oxide Cathode via an Integrated Strategy. *Adv. Funct. Mater.* **2019**, *29*, No. 1806706.
(42) Hu, G.; Zhang, M.; Wu, L.; Peng, Z.; Du, K.; Cao, Y. Enhanced Electrochemical Performance of $LiNi_{0.5}Co_{0.2}Mn_{0.3}O_2$ Cathodes Produced via Nanoscale Coating of $Li^+$-Conductive $Li_2SnO_3$. *Electrochim. Acta* **2016**, *213*, 547−556.
(43) Mou, J.; Deng, Y.; Song, Z.; Zheng, Q.; Lam, K. H.; Lin, D. Excellent Rate Capability and Cycling Stability in $Li^+$-Conductive $Li_2SnO_3$-Coated $LiNi_{0.5}Mn_{1.5}O_4$ Cathode Materials for Lithium-Ion Batteries. *Dalton Trans.* **2018**, *47*, 7020−7028.
(44) Lu, F.; Yang, J.; Zhou, L.; Wang, X.; Yang, Y.; Li, J. Enhanced Electrochemical Performance and Mechanism Study of $AgLi_{1/3}Sn_{2/3}O_2$ for Lithium Storage. *Chin. Chem. Lett.* **2019**, *30*, 2017−2020.
(45) Zhang, W.; Leichtweiß, T.; Culver, S. P.; Koerver, R.; Das, D.; Weber, D. A.; Zeier, W. G.; Janek, J. The Detrimental Effects of Carbon Additives in $Li_{10}GeP_2S_{12}$-Based Solid-State Batteries. *ACS Appl. Mater. Interfaces* **2017**, *9*, 35888−35896.
(46) Hakari, T.; Deguchi, M.; Mitsuhara, K.; Ohta, T.; Saito, K.; Orikasa, Y.; Uchimoto, Y.; Kowada, Y.; Hayashi, A.; Tatsumisago, M. Structural and Electronic-State Changes of a Sulfide Solid Electrolyte During the Li Deinsertion−Insertion Processes. *Chem. Mater.* **2017**, *29*, 4768−4774.
(47) Strauss, F.; Bartsch, T.; de Biasi, L.; Kim, A. Y.; Janek, J.; Hartmann, P.; Brezesinski, T. Impact of Cathode Material Particle Size on the Capacity of Bulk-Type All-Solid-State Batteries. *ACS Energy Lett.* **2018**, *3*, 992−996.
(48) Sakuda, A.; Takeuchi, T.; Kobayashi, H. Electrode Morphology in All-Solid-State Lithium Secondary Batteries Consisting of $LiNi_{1/3}Co_{1/3}Mn_{1/3}O_2$ and $Li_2S-P_2S_5$ Solid Electrolytes. *Solid State Ionics* **2016**, *285*, 112−117.

(49) Wang, J.; Zhang, Z.; Han, J.; Wang, X.; Chen, L.; Li, H.; Wu, F. Interfacial and Cycle Stability of Sulfide All-Solid-State Batteries with Ni-Rich Layered Oxide Cathodes. *Nano Energy* **2022**, *100*, No. 107528.
(50) Quemin, E.; Dugas, R.; Chaupatnaik, A.; Rousse, G.; Chometon, R.; Hennequart, B.; Tarascon, J.-M. An Advanced Cell for Measuring In Situ Electronic Conductivity Evolutions in All-Solid-State Battery Composites. *Adv. Energy Mater.* **2023**, *13*, No. 2301105.
(51) Otoyama, M.; Yamaoka, T.; Ito, H.; Inagi, Y.; Sakuda, A.; Tatsumisago, M.; Hayashi, A. Visualizing Local Electrical Properties of Composite Electrodes in Sulfide All-Solid-State Batteries by Scanning Probe Microscopy. *J. Phys. Chem. C* **2021**, *125*, 2841−2849.
(52) Kim, T.; Kim, K.; Lee, S.; Song, G.; Jung, M. S.; Lee, K. T. Thermal Runaway Behavior of $Li_6PS_5Cl$ Solid Electrolytes for $LiNi_{0.8}Co_{0.1}Mn_{0.1}O_2$ and $LiFePO_4$ in All-Solid-State Batteries. *Chem. Mater.* **2022**, *34*, 9159−9171.
(53) Chae, O. B.; Park, S.; Ryu, J. H.; Oh, S. M. Performance Improvement of Nano-Sized Zinc Oxide Electrode by Embedding in Carbon Matrix for Lithium-Ion Batteries. *J. Electrochem. Soc.* **2013**, *160*, No. A11, DOI: 10.1149/2.024301jes.
(54) Jun, S.; Nam, Y. J.; Kwak, H.; Kim, K. T.; Oh, D. Y.; Jung, Y. S. Operando Differential Electrochemical Pressiometry for Probing Electrochemo-Mechanics in All-Solid-State Batteries. *Adv. Funct. Mater.* **2020**, *30*, No. 2002535.
(55) Jun, S.; Lee, G.; Song, Y. B.; Lim, H.; Baeck, K. H.; Lee, E. S.; Kim, J. Y.; Kim, D. W.; Park, J. H.; Jung, Y. S. Interlayer Engineering and Prelithiation: Empowering Si Anodes for Low-Pressure-Operating All-Solid-State Batteries. *Small* **2024**, *n/a*, No. 2309437.
(56) Ohzuku, T.; Ueda, A.; Yamamoto, N. Zero-Strain Insertion Material of $Li[Li_{1/3}Ti_{5/3}]O_4$ for Rechargeable Lithium Cells. *J. Electrochem. Soc.* **1995**, *142*, No. 1431, DOI: 10.1149/1.2048592.
(57) Kwak, H.; Wang, S.; Park, J.; Liu, Y.; Kim, K. T.; Choi, Y.; Mo, Y.; Jung, Y. S. Emerging Halide Superionic Conductors for All-Solid-State Batteries: Design, Synthesis, and Practical Applications. *ACS Energy Lett.* **2022**, *7*, 1776−1805.
(58) Asano, T.; Sakai, A.; Ouchi, S.; Sakaida, M.; Miyazaki, A.; Hasegawa, S. Solid Halide Electrolytes with High Lithium-Ion Conductivity for Application in 4 V Class Bulk-Type All-Solid-State Batteries. *Adv. Mater.* **2018**, *30*, No. 1803075.
(59) Zhang, W.; Schröder, D.; Arlt, T.; Manke, I.; Koerver, R.; Pinedo, R.; Weber, D. A.; Sann, J.; Zeier, W. G.; Janek, J. Electro)chemical Expansion During Cycling: Monitoring the Pressure Changes in Operating Solid-State Lithium Batteries. *J. Mater. Chem. A* **2017**, *5*, 9929−9936.


https://doi.org/10.1021/acs.chemmater.4c00629
*Chem. Mater.* 2024, 36, 5215−5227